




Bone-mimetic porous hydroxyapatite/whitlockite scaffolds: preparation, characterization and interactions with human mesenchymal stem cells

Leonard Bauer^{1,*} , Maja Antunović¹, Anamarija Rogina¹, Marica Ivanković¹, and Hrvoje Ivanković¹

¹ Faculty of Chemical Engineering and Technology, University of Zagreb, Marulićev trg 19, HR-10000 Zagreb, Croatia

Received: 8 June 2020

Accepted: 21 October 2020

Published online:

4 November 2020

© Springer Science+Business Media, LLC, part of Springer Nature 2020

ABSTRACT

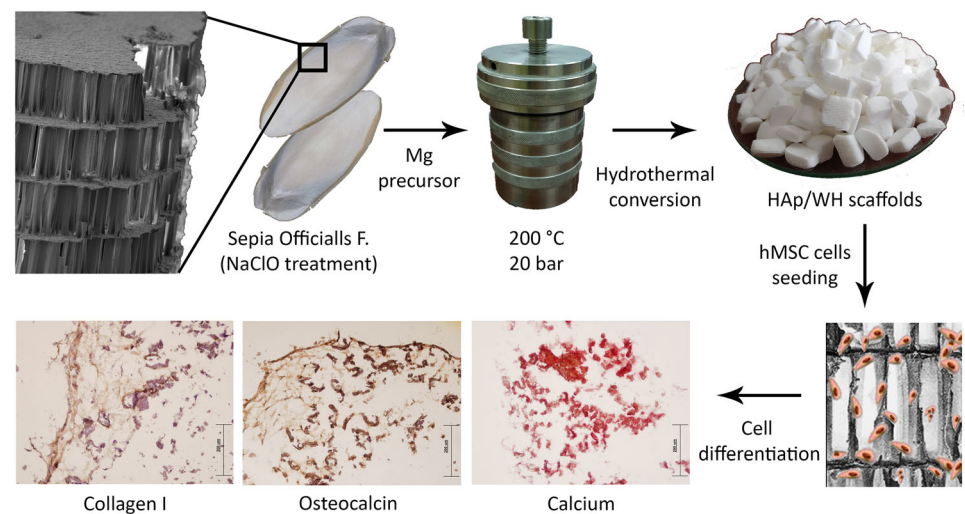
Bone-mimetic highly porous Mg-substituted calcium phosphate scaffolds, composed of hydroxyapatite (HAP) and whitlockite (WH), were synthesized by hydrothermal method at 200 °C, using calcium carbonate skeletons of cuttlefish bone, ammonium dihydrogenphosphate ($\text{NH}_4\text{H}_2\text{PO}_4$) and magnesium chloride hexahydrate ($\text{MgCl}_2 \times 6\text{H}_2\text{O}$) or magnesium perchlorate ($\text{Mg}(\text{ClO}_4)_2$) as reagents. The effect of Mg content on the compositional and morphological properties of scaffolds was studied by means of X-ray diffraction, Fourier transform infrared spectroscopy, thermogravimetric analysis and scanning electron microscopy (SEM) with energy-dispersive X-ray analysis. Structural refinements performed by Rietveld method indicated that Mg^{2+} ions were preferentially incorporated into the WH phase. SEM images of all prepared scaffolds showed that the interconnected structure of the cuttlefish bone was completely maintained after the hydrothermal synthesis. Results of compression tests showed a positive impact of the whitlockite phase on the mechanical properties of scaffolds. Human mesenchymal stem cells (hMSCs) were cultured on scaffolds in osteogenic medium for 21 days. Immunohistochemical staining showed that Mg-CaP scaffolds with the HAP:WH wt ratio of 90:10 and 70:30 exhibited higher expression of collagen type I and osteocalcin than pure HAP scaffold. Calcium deposition was confirmed by Alizarin Red staining. Positive effect of Mg^{2+} ions on the differentiation of hMSCs on porous 3D scaffolds was also confirmed by reverse transcription-quantitative polymerase chain reaction analysis.

Handling Editor: Christopher Blanford.

Address correspondence to E-mail: lbauer@fkit.hr

<https://doi.org/10.1007/s10853-020-05489-3>

GRAPHICAL ABSTRACT



Introduction

Over the last three decades, calcium phosphate (CaP) ceramics have been extensively studied and widely used as bone substitute materials [1–4]. In addition to the most researched hydroxyapatite (HAP, $\text{Ca}_{10}(\text{PO}_4)_6(\text{OH})_2$), tricalcium phosphate (β -TCP, $\text{Ca}_3(\text{PO}_4)_2$) and the biphasic mixture of HAP and β -TCP (BCPs) have also attracted considerable attention. In order to better mimic natural bone mineral, ionic substitutions within the apatite lattice have been widely employed. Several reviews have been published on the preparation of ion substituted calcium phosphate materials [5–8].

Mg^{2+} ion plays an important role in bone metabolism [9], which is the reason why it has attracted such remarkable interest. Magnesium deficiency can result in decreased bone mass, reduced bone growth and osteoporosis.

To incorporate Mg^{2+} inside the HAP crystal lattice, the wet chemical precipitation method has mostly been employed [10–16]. In some studies, the mechanochemical hydrothermal route [17] and the sol–gel method [18] were applied, as well. The reported studies [19, 20], show that Mg substitution

for Ca in the hydroxyapatite structure occurs over a limited composition range (up to about 10 wt%), the main portion being surface bound or present in a separate phase. Different results on the favoured Ca position for Mg^{2+} replacement are reported. Studies of Laurencin et al. [21], performed on a $\sim 10\%$ Mg-substituted HAP by high magnetic field ^{43}Ca solid state NMR and Ca *K*-edge XAS, brought direct evidence of the preferential substitution of Mg in the Ca(II) position.

Mg^{2+} ions play a key role in the formation of whitlockite [22, 23]. Until recently, whitlockite (WH, $\text{Ca}_9\text{Mg}(\text{HPO}_4)(\text{PO}_4)_6$), albeit the second most abundant mineral in human bone [24, 25], has not been extensively studied in the context of bone tissue engineering.

The crystal structure of WH is analogous to that of β -TCP [26], whereby the term “whitlockite” is very often used to designate β -TCP. Although the distinction between the two has been clarified [27], the terms have been used interchangeably and synonymously. This may cause confusion, and attention should be paid to the proper usage of these two terms. The term “whitlockite” should be used for the mineral itself or for similar synthetic materials in which Mg^{2+} and HPO_4^{2-} ions are present.

Jang et al. [22, 23] demonstrated that pure WH nanoparticles can be formed in Mg^{2+} -rich and acidic pH solutions. Compared to HAP, WH showed higher compressive strength and superior osteogenic capability both in vitro and in vivo [28, 29]. WH is more soluble than HAP in physiological conditions and can continuously release Mg^{2+} ions that can enhance the growth and osteogenic differentiation of stem cells [29, 30]. In addition, a negatively charged surface of WH enables positively charged osteogenic proteins such as bone morphogenetic protein (BMP) to be adsorbed on its surface by electrostatic interactions [29].

A range of biphasic mixtures of Mg-HAP and whitlockite have been prepared via continuous hydrothermal flow synthesis [31]. Biphasic HAP/WH materials have recently been prepared from natural sources (chicken bone), as well [32]. It has been hypothesized that the BCP mixture of HAP and WH may mimic natural bone better than each phase alone. It has recently been shown that osteogenic activity increases when WH and HAP coexist at a ratio of approximately 1:3, which is a similar ratio to that in native human bone [33].

This study is a continuation of our previous work [34–38] on the preparation of bone-mimetic calcium phosphate materials derived from cuttlefish bone, where natural aragonite was hydrothermally transformed into HAP at 200 °C and its highly interconnected macroporosity was preserved.

Cuttlefish bone is a low-cost, worldwide available natural cellular material possessing high stiffness, high porosity (~ 90%) and high permeability. High porosity and interconnected pores are essential for bone tissue engineering scaffolds, facilitating migration and a uniform distribution of cells, vascularization and adequate transport of nutrients, oxygen and metabolic waste products.

Hydrothermal synthesis is one-step procedure performed at relatively mild conditions (reaction temperatures < 300 °C) compared to conventional ceramic process of solid state reaction. Moreover, it is simple in terms of the instrumentation, inexpensive in terms of energy and material precursors compared with other solution synthesis methods. It is more environmentally benign than many other methods.

The aim of this work is to study the effects of the Mg^{2+} ion content on the microstructural, mechanical

and biological properties of calcium phosphates derived from cuttlebone. Porous biphasic HAP/WH scaffolds with different HAP:WH ratios were synthesized by changing the content of Mg^{2+} ions. To the best of our knowledge, no study on hydrothermal synthesis and characterization of HAP/WH biomaterials, derived from cuttlefish bone, has been reported thus far.

Materials and methods

Scaffold preparation

Cuttlefish bones (*Sepia Officinalis L.*) from the Adriatic Sea were used as a calcium source for the hydrothermal synthesis of Mg-substituted calcium phosphates. The cuttlebones of 15 ± 1 cm in total length were selected. The use of organisms from the same semi-enclosed marine environment, and of the same size, made it possible to get porous scaffolds with a comparable microstructure (porosity and pore size). Dorsal shield was mechanically removed from the cuttlefish bones. Internal lamellae matrix of the bones was cut into pieces ($\approx 2 \text{ cm}^3$) and treated with an aqueous solution of sodium hypochlorite (NaClO, 13% active chlorine, Gram-mol) at room temperature for 48 h and repeatedly washed with boiling demineralized water to remove the organic component. As-prepared pieces of cuttlefish bone were sealed with the required quantity of a 0.6 mol dm^{-3} aqueous solution of ammonium dihydrogenphosphate ($NH_4H_2PO_4$, 99% Fisher Scientific) and magnesium chloride hexahydrate ($MgCl_2 \times 6H_2O$, Kemig, Ph.Eur.9.0) or magnesium perchlorate ($Mg(ClO_4)_2$, 99% Sigma-Aldrich) in a TEFLON-lined stainless steel pressure vessels at 200 °C for 48 h. The self-generated pressure inside the reactor reached up to 20 bars. After hydrothermal treatment, the resulting pieces of scaffolds were washed with boiling demineralized water, dried at 105 °C and stored for further analysis. All calculations for stoichiometric ratios and preparation of starting reaction mixtures were based on the formula for Mg-substituted hydroxyapatite, i.e. $Ca_{10-x}Mg_x(PO_4)_6(OH)_2$, with the constant $(Ca + Mg)/P$ molar ratio of 1.67. Five samples with different molar contents of Mg ($x = 0, 0.1, 0.25, 0.5, 0.1$) have been prepared and labelled as CaP, 1-Mg-CaP, 2.5-Mg-CaP, 5-Mg-CaP and 10-Mg-CaP, respectively. The number before Mg-CaP is the

Table 1 Nominal composition of prepared samples

Sample code	Mg/(Ca + Mg) (mol%)	(Ca + Mg)/P
CaP	0	1.67
1-Mg-CaP	1	1.67
2.5-Mg-CaP	2.5	1.67
5-Mg-CaP	5	1.67
10-Mg-CaP	10	1.67

nominal Mg mol% value expected to be substituted into hydroxyapatite (in place of Ca) (Table 1).

XRD analysis and Rietveld refinement

Samples were characterized with the XRD Shimadzu 6000 diffractometer (Bragg–Brentano geometry with $\text{CuK}\alpha$ source) with a scintillation detector and a goniometer radius of 185 mm. Used divergence and scattering slit were 1° in the primary beam, soller slits were 4.6° , while 0.30 mm receiving slit and secondary graphite monochromator were in the secondary beam. Samples were scanned in the range of diffraction angles between 5 and 70° with a 2θ step of $0.02^\circ 2\text{ s}^{-1}$ for qualitative analysis and $0.02^\circ 10\text{ s}^{-1}$ with the addition of known addition of silicon standard into the pure HAP sample for HAP structure refinement. For the XRD measurements, powdered samples were prepared by hand grinding of whole 3D scaffold in ethanol using corundum mortar and pestle. Identification of the phases was performed by comparing the experimental XRD patterns to standards compiled by the International Centre for Diffraction Data (ICDD) using the card 41–1475 for aragonite, 09–432 for HAP and 70–2064 for whitlockite.

The Rietveld structure refinement was carried out using a program DIFFRAC.SUITE TOPAS v.5.0 (Bruker) [39]. The background was described by a Chebyshev polynomial equation of the 5th order. The peak profiles were fitted with pseudo-Voigt function. The structure of Holly Springs HAP was used as a starting model without the inclusion of CO_3^{2-} in the structure [40]. Unit-cell parameters, positional parameters and occupancies were varied [41]. The structure of synthetic whitlockite, $\text{Ca}_{18}\text{Mg}_2(\text{HPO}_4)_2(\text{-PO}_4)_{12}$, refined by Gopal [42] and structure of aragonite [43] were used as models for remaining crystal phases.

FTIR analysis

Fourier transform infrared spectra (FTIR) were performed by attenuated total reflectance (ATR) spectroscopy of solids with a diamond crystal (Bruker Vertex 70) at 20°C over the spectral range of $400\text{--}4000\text{ cm}^{-1}$, with 32 scans and 4 cm^{-1} resolution.

SEM–EDX analysis

Morphology of scaffolds was examined by scanning electron microscopy (SEM Tescan Vega III Easyprobe). An energy-dispersive X-ray (EDX) spectrometer connected to the SEM (SEM ISIDS-130) has been used to determine the elemental composition of scaffolds. Prior to the SEM and EDX analysis, the samples were sputtered with gold and palladium.

Thermal analysis

Thermogravimetric analysis (TGA) was performed on a Netzsch STA 409 with a constant synthetic air-flow of $30\text{ cm}^3\text{ min}^{-1}$ from 40°C to 1200°C at a heating rate of $10^\circ\text{C min}^{-1}$.

MTT viability assay

3-(4,5-dimethylthiazol-2-yl)-2,5-diphenyltetrazolium bromide (MTT) assay was used to determine the potential cytotoxic effect of prepared scaffolds. The assay was performed using human embryonic kidney (HEK293) cell line by indirect contact cell culture. The cells were seeded at a density of $3000\text{ cells } 200\text{ }\mu\text{L}^{-1}$ in tissue culture-treated 96-well plate (Sarsted) in triplicates and grown in Dulbecco's modified Eagle medium with 4500 mg L^{-1} glucose (DMEM high glucose) (Lonza) containing 10% fetal bovine serum (FBS) (Gibco), 100 U mL^{-1} penicillin and $100\text{ }\mu\text{g mL}^{-1}$ streptomycin (Sigma-Aldrich).

Prior to preparing sample extracts, powders of samples were disinfected with alcohol (96% w/v ethanol) for 4 h, centrifuged for 5 min at $1500 \times G$ and extensively washed with sterile phosphate-buffered saline (PBS) three times. Then, disinfected samples were resuspended in culture medium at concentrations of 10 mg mL^{-1} and incubated at 4°C for 7 days. After the incubation period, extracts were centrifuged for 5 min at $1500 \times G$ and used for viability testing.

After one day of cell culture, the growth medium was replaced with extracts and incubated for 72 h in a 5% CO₂ humidified atmosphere at 37 °C. A fresh growth medium was added to untreated control cells as well, which were defined as 100% viable. After the incubation period, 40 µL of MTT (Sigma-Aldrich) was added to each well at a concentration of 0.5 mg mL⁻¹. After 4 h of incubation period at 37 °C, formazan crystals were dissolved by adding 170 µL of DMSO to each well. After 20 min at room temperature, the absorbance was measured on a microplate reader (GloMax-Multi detection system, Promega) at 560 nm. The percentage of viable cells cultured with sample extracts was calculated with respect to untreated cells.

Isolation and proliferation of hMSCs

Primary isolation and culture of hMSCs were performed as described in detail earlier [44, 45]. Briefly, bone marrow aspirates were added to DMEM with 1000 mg L⁻¹ glucose (DMEM low glucose, Lonza) containing 10% FBS (Gibco), 100 U mL⁻¹ penicillin and 100 µg mL⁻¹ streptomycin (Lonza). The suspension was centrifuged while pelleted cells were washed in PBS followed by straining through a cell strainer (70 µm, BD Biosciences). The isolated cells were plated at a density of 1 × 10⁸ in proliferation medium DMEM low glucose, supplemented with 10% FBS, 100 U mL⁻¹ penicillin, 100 µg mL⁻¹ streptomycin and 10 ng mL⁻¹ human fibroblast growth factor 2 (FGF2, Gibco), and kept in a humidified incubator at 37 °C with a 5% CO₂ supply. After 24 h, the media was replaced and the attached cells were grown. When hMSCs became 80% confluent, they were detached with 0.25% trypsin/EDTA (Sigma-Aldrich) and then subcultured for expansion. The proliferation medium was changed every 2–3 days.

Osteogenic differentiation of hMSCs cultured in 3D static conditions

Prior to the cell seeding, scaffolds were sterilized with γ -rays (25 kGy). The cells were seeded on the scaffolds (5 mm of diameter cut perpendicular to lamellae structure) at a density of 5 × 10⁵ cells 200 µL⁻¹ of proliferation medium in tissue culture non-treated 96-well plates (Sarsted) in triplicates. Following 24 h, the proliferation medium was

changed to the osteogenic induction medium containing Minimum Essential Medium-Alpha Eagle (α -MEM, Lonza), 10% FBS, 1% penicillin/streptomycin, 50 µg mL⁻¹ ascorbic acid (Sigma-Aldrich), 4 mmol L⁻¹ β -glycerophosphate (Sigma-Aldrich) and 1 × 10⁻⁷ mol L⁻¹ dexamethasone (Sigma-Aldrich). The medium was exchanged every 2 days during 14 and 21 days, respectively.

Immunohistochemical detection of collagen type I and osteocalcin

Expression of osteogenic matrix markers collagen type I and osteocalcin was chosen for immunohistochemical analysis to assess the osteogenic differentiation capacity of hMSCs cultured on the scaffolds. Sections were prepared and treated as described earlier [45]. After 14 and 21 days of osteogenic differentiation, the scaffolds were removed from the culture medium and fixed in 4% paraformaldehyde. After equilibration in PBS buffered with 30% sucrose for 48 h, the samples were embedded in Tissue-Tek (O.C.T. compound, Sakura, CA, USA) and frozen at -80 °C. 10-µm-thick sections (cryostat, Leica, Wetzlar, Germany) were mounted on Superfrost Plus slides (Thermo Fisher Scientific). Scaffolds without cells but in the same culture conditions were used as blanks. The sections were subjected to proteinase K (Proteinase K Ready to use, Dako, Togo) antigen retrieval for 3 min at room temperature. Endogenous peroxidase activity was blocked with 3% H₂O₂ in PBS for 3–6 min. Nonspecific binding sites were blocked with 10% goat serum (Dako) in PBS for 60 min at room temperature. Sections were then incubated with primary antibody (anti-collagen I, Abcam, Cambridge, UK), diluted 1:400 or anti-osteocalcin (FL-100, Santa Cruz Biotechnology, Dallas, TX, USA) and diluted 1:50, respectively, with 1% goat serum in PBS, overnight at 4 °C. After washing, the signal was detected with EnVision Detection Systems Peroxidase/DAB, Rabbit/Mouse (Dako), according to the manufacturer instructions. Hematoxylin was used as a counterstain. Negative controls were processed in the same way with the omission of the primary antibody. Human bone was used as a positive control. All slides were visualized using an Olympus BX51 microscope and images captured by digital camera.

Alizarin red staining

The extent of extracellular matrix calcification of hMSCs on scaffolds was evaluated at day 14 and day 21 by using the Alizarin Red S (Sigma-Aldrich) staining kit. Specimens were stained for 2 min with 2% (w/v) Alizarin Red solution (pH 4.4), dehydrated and finally mounted onto glass slides using Biognost mounting medium. Photomicrographs of the grafts were taken using a digital camera on an Olympus BX51 microscope.

Isolation of total RNA and quantitative reverse transcription PCR (RT-qPCR) analysis

Total RNA was collected from 14- and 21-day-old tissue cultures using TRIzol reagent (Invitrogen Life Technologies) according to manufacturer's instructions. Briefly, the samples were washed in cold PBS, homogenized in 1 mL TRIzol reagent (Thermo fisher) using mixer mill (Retsch) at 15 Hz for 3 min and mixed with chloroform. In the upper aqueous phase containing RNA, 50 mmol L⁻¹ EDTA was added following RNA precipitation with isopropanol. 0.5 µg of total RNA was treated with DNase I by adding 10 × DNase I reaction buffer and 50 mmol L⁻¹ EDTA (all Applied Biosystems). DNase I-treated RNA was then used to synthesize cDNA using High-Capacity cDNA Reverse Transcription Kit with RNase Inhibitor (Applied Biosystems). Reverse transcription was performed in thermomixer (Eppendorf) at the following conditions: 10 min at 25 °C, 120 min at 37 °C and 5 min at 85 °C. Power SYBR green PCR master mix (Applied Biosystems) were used to analyse the expression of commercially available primers (Sigma-Aldrich) for: alkaline phosphatase (ALPL), bone sialoprotein (BSP) and dentin matrix protein 1 (DMP1). RT-qPCR was performed on 7500 Fast Real-Time PCR System (Applied Biosystems). The PCR conditions were as follows: 10 min at 95 °C for 1 cycle, 15 s at 95 °C and 1 min at 57 °C for 40 cycles. Expression levels were normalized to β-actin. Relative expression of target genes was calculated using the ΔΔCt method.

Mechanical testing

Mechanical properties of selected scaffolds were determined by a static compression test using the

Microtest standard instrument (Microtest S.A.) with 500 N loading cell and a cross-head velocity of 0.2 mm min⁻¹. Samples (*n* = 9) of scaffolds (4–6 × 4–6 × 4–6 mm) were examined by dry test and compressive load was applied perpendicular to lamellae of each specimen. The elastic compression modulus was determined as the slope of the initial linear range of stress–strain curves.

Statistical analysis

Significant difference between two groups was determined by statistical analysis using a one-way ANOVA test, with the *p* < 0.05 and *p* < 0.01 values as statistically significant.

Results

The comparison of scaffolds characterization prepared with different Mg precursors (magnesium chloride hexahydrate or magnesium perchlorate) showed very small differences that were not noticeable through graphical representation. Therefore, in the following sections only the results corresponding to the scaffolds prepared with magnesium perchlorate (with the exception of XRD quantitative results and MTT assay) are presented.

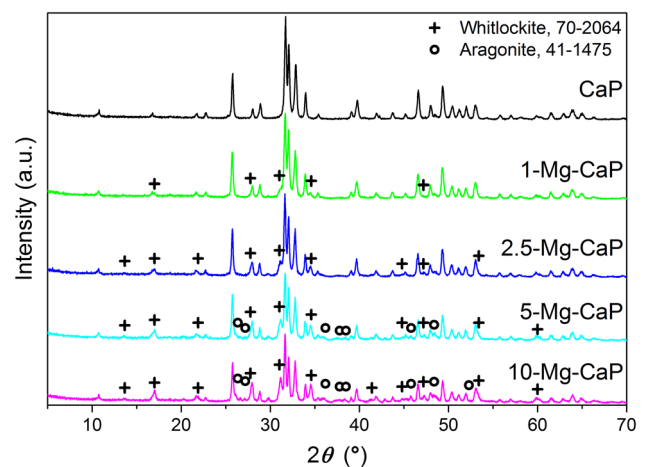


Figure 1 XRD patterns of prepared scaffolds. The 2θ positions of whitlockite and aragonite are marked with (+) and (o), respectively; the HAP (09–432) positions were not marked for the purpose of clarity.

XRD analysis and Rietveld refinement

XRD patterns of prepared scaffolds are shown in Fig. 1.

The XRD data for the sample CaP gave a good match to the line pattern for crystalline HAP (ICDD 09–432). Sample 1-Mg-CaP was identified as a biphasic mixture, with a good match to the pattern for HAP and whitlockite (ICDD 70–2064). In samples 2.5-Mg-CaP, 5-Mg-CaP and 10-Mg-CaP, in addition to HAP and WH patterns, low intensity peaks with a good match to the diffraction lines of aragonite (ICDD 41–1475) were observed, as well.

Rietveld refinement analysis was performed on XRD patterns of all prepared samples to determine unit-cell dimensions, crystallite size and weight percent proportions of detected phases. Regarding the refinement of the hydroxyapatite structure, different constraints (A, B, C, D) on the value of P1, O1, O2 and O3 occupancies, and/or H1 and O4 occupancies have been applied (see Table 2 and additional Tables given in Online Resource 1). In the refinement A, P1, O1, O2 and O3 occupancy parameters were allowed to vary, but constrained to the same value (see Table A) in Online Resource 1). The same constraint was applied to H1 and O4 occupancy parameters. In the refinement B, no constraint on the value of P1, O1, O2 and O3 occupancy parameters was applied while H1 and O4 occupancy parameters have been constrained to the same value (Table B) in Online Resource 1). The only difference between the refinement A and the refinement C is that H1 and O4 occupancy parameters were fixed to the value of 0.5 (Table C) in Online Resource 1). In the refinement D, no constraint on the

value of P1, O1, O2 and O3 occupancy parameters was applied, but the maximum value of the H1 and O4 occupancy parameter was set to 0.5 (see Table 2). The refined hydroxyapatite structure of the sample CaP was used as the initial structure for refinements of magnesium-substituted hydroxyapatite structure in samples 1-Mg-CaP, 2.5-Mg-CaP, 5-Mg-CaP and 10-Mg-CaP, where only unit-cell parameters were refined. The calculation flow of the Rietveld refinement is given in Fig. 2. Positional parameters and occupancies in the refined HAP structure, obtained in refinements D, are given in Table 2.

Results of quantitative analysis of samples prepared by two different Mg precursors are compared in Table 3. As shown in Table 3, the addition of magnesium in the starting reaction mixture resulted in a decrease in HAP content and an increase in the content of whitlockite and nontransformed aragonite. When magnesium chloride hexahydrate was used as a precursor, higher content of nontransformed aragonite was estimated in the scaffolds 5-Mg-CaP and 10-Mg-CaP. In addition, the samples 5-Mg-CaP and 10-Mg-CaP showed high intensity maximum on XRD diffractogram at around $2\theta = 10.0^\circ$ assigned to 010 *hkl* of dittmarite ($\text{NH}_4\text{MgPO}_4 \times \text{H}_2\text{O}$, ICDD 34–1491) (see Figs and discussion given in Online Resource 2).

Rietveld refinements ended with the resultant weighted profile factors, R_{wp} , in the range between 6 and 11% (Table 3) indicating a good agreement between the calculated and the experimental data, as illustrated in Fig. 3a, b.

The calculated molar ratio Ca/P for HAP in refinements A to D ranges between 1.71 and 1.80 which is higher than the stoichiometric value (1.67) indicating the deficiency of PO_4^{3-} and the presence of carbonate ion in the structure, which is confirmed by FTIR data shown later. Since FTIR results showed that with the appearance and increase in whitlockite content (i.e. the reduction in hydroxyapatite content) in the prepared samples, the intensity of CO_3^{2-} vibrational bands reduces, we supposed that CO_3^{2-} is mostly placed in the apatite phase.

Supposing that the ratio of calcium sites per unit cell to the sum of PO_4^{3-} and CO_3^{2-} is ten to six, the amount of CO_3^{2-} incorporated into the structure of HAP was calculated. The formula given by the unit-cell content for hydroxyapatite sample with refined structure D is:

Table 2 Values of positional parameters and occupancies in refined HAP structure

	Np	<i>x</i>	<i>y</i>	<i>z</i>	Occ
Ca1	4	1/3	2/3	0.0009	0.8306
Ca2	6	0.2469	0.9920	1/4	0.8624
P1	6	0.3956	0.3673	1/4	0.7854
O1	6	0.3307	0.4818	1/4	0.8744
O2	6	0.5794	0.4613	1/4	0.8643
O3	12	0.3371	0.2537	0.0697	0.8198
O4	4	0	0	0.1809	0.5000*
H1	4	0	0	0.0050	0.5000*

*The H1 and O4 occupancy parameters refined setting the maximum parameter value to 0.5000

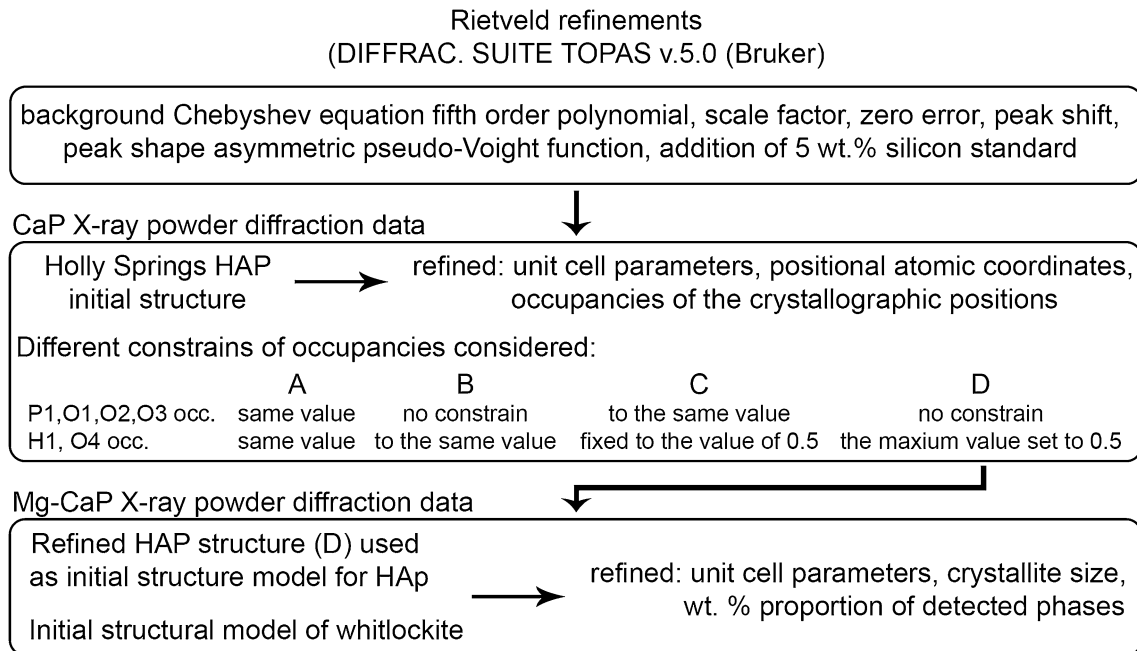
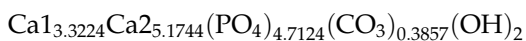


Figure 2 Calculation flow of the Rietveld refinement where basic starting refinement parameters are visible in the top section of chart, conditions and refined parameters for CaP in the middle and for Mg-CaP samples at the bottom section of flow chart.

Table 3 Results of quantitative analysis performed by Rietveld refinement of the XRD data

Precursor Sample	Magnesium perchlorate				Magnesium chloride hexahydrate			
	Wt%				Wt%			
	HAP	WH	Aragonite	Rwp	HAP	WH	Aragonite	Rwp
CaP	100	0	0	5.98				
1-Mg-CaP	90.48	9.52	0	6.06	87.10	12.90	0	6.65
2.5-Mg-CaP	87.03	11.19	1.78	6.41	79.10	20.20	0.70	7.87
5-Mg-CaP	69.25	28.84	1.91	7.05	72.15	23.34	4.64	7.67
10-Mg-CaP	53.61	38.64	7.76	7.24	55.76	31.85	11.95*	11.03

*See Online Resource 2.



It should be noted that the structure is slightly positively charged (+ 0.085). For refined structures A, B and C, the formulas are $\text{Ca}_{13.9424}\text{Ca}_{26.138}(\text{PO}_4)_{5.8932}(\text{CO}_3)_{0.1550}(\text{OH})_{2.4764}$, $\text{Ca}_{13.9592}\text{Ca}_{26.162}(\text{PO}_4)_{5.637}(\text{CO}_3)_{0.4357}(\text{OH})_{2.4676}$ and $\text{Ca}_{13.3352}\text{Ca}_{25.2260}(\text{PO}_4)_{4.9860}(\text{CO}_3)_{0.1507}(\text{OH})_2$, while the charge imbalance is - 0.3052, - 0.0076 and - 0.1496, respectively.

Rietveld refinements showed that different constraints had a negligible effect on the unit-cell dimensions derived from the data (compare Table 4 and the data given in online resource 3). As shown in Table 4, the lattice parameters and unit-cell volume of HAP in the prepared CaP samples show no

systematic change with increased levels of magnesium in the samples.

The refinement of the whitlockite structure revealed a decrease in the lattice parameters a and c , and unit-cell volume with the increase in magnesium content (exception is the sample 5-Mg-CaP), suggesting the substitution of the larger calcium ion (ionic radius 0.99 Å) with the smaller magnesium ion (ionic radius 0.65 Å) that induced a lattice contraction. The calculated Mg occupancies in the WH phase for samples 1-, 2.5-, 5- and 10-Mg-CaP were 0.9363, 0.9863, 1.054 and 1.053, respectively.

The crystallite size of the HAP phase in the prepared samples ranged from 55 to 96 nm. The very

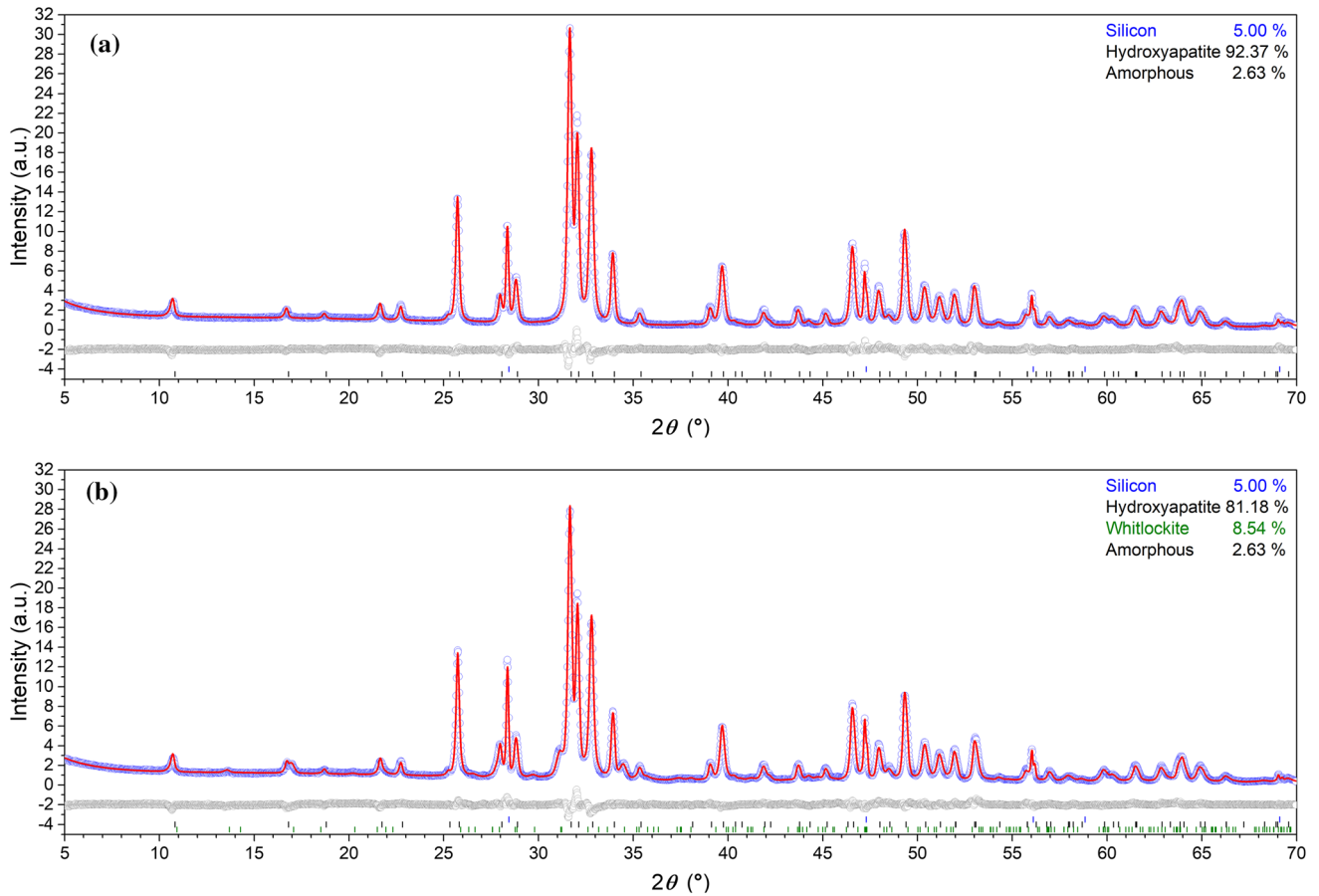


Figure 3 Rietveld output of X-ray powder diffraction pattern of **a** CaP scaffold and **b** 1-Mg-CaP scaffold, with the addition of 5 wt% of silicon standard, under the refinement *D* conditions. The red solid line is the best fit of the profile, and blue circles are the experimental data. The difference between the experimental and

fitted patterns is shown under the diffraction pattern with grey circles. Line markers on the bottom of the figure indicate the position of Bragg reflections for silicon (blue line markers), hydroxyapatite (black line markers) and whitlockite (green line markers).

Table 4 Unit-cell parameters of HAP and WH phase obtained by Rietveld refinement of the XRD data

Sample	Hydroxyapatite				Whitlockite			
	Cell parameters (P63/m)				Cell parameters (R3C)			
	a (Å)	c (Å)	Cell vol. (Å ³)	Cryst. sizeLvol-IB (nm)	a (Å)	c (Å)	Cell vol. (Å ³)	Cryst. Size Lvol-IB (nm)
CaP	9.4330	6.8981	531.573	55.633	–	–	–	–
1-Mg-CaP	9.4325	6.8964	531.382	67.307	10.3795	37.2133	3472.044	24.680
2.5-Mg-CaP	9.4297	6.8987	531.238	70.922	10.3751	37.2076	3468.537	23.682
5-Mg-CaP	9.4340	6.8944	531.400	91.867	10.3716	37.2386	3469.069	22.631
10-Mg-CaP	9.4361	6.8903	531.315	74.950	10.3570	37.2020	3455.939	25.010

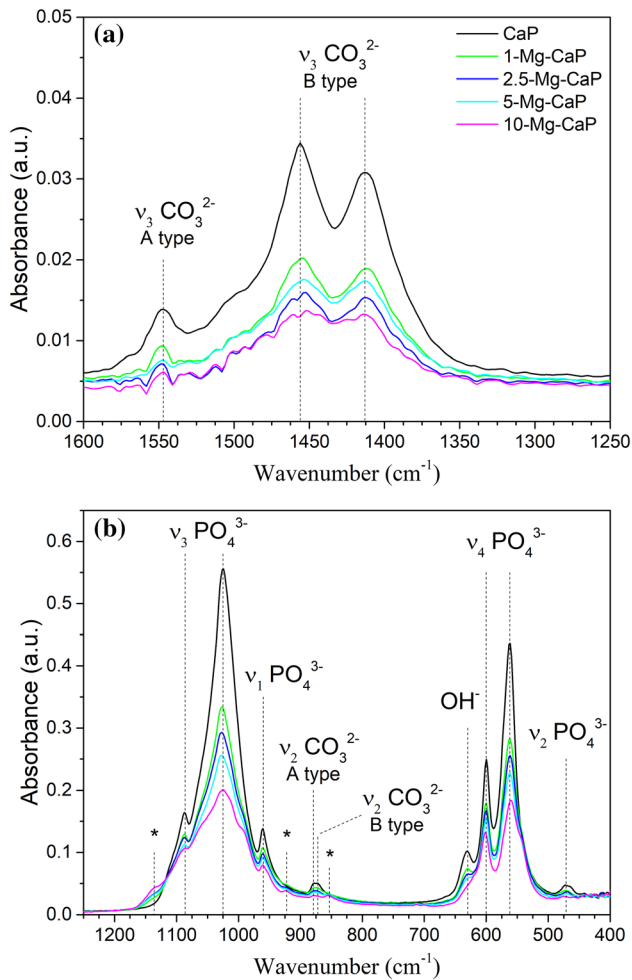


Figure 4 FTIR spectra of prepared samples over the spectral range of **a** 1600 to 1250 cm^{-1} and **b** 1250 to 400 cm^{-1} .

small difference in crystallite size (ranging between 23 and 25 nm) was obtained for the WH phase in all prepared Mg-substituted samples.

FTIR analysis

The Fourier transform infrared spectra of prepared samples are presented in Fig. 4a, b.

The most intense bands at 1086 and 1022 cm^{-1} are assigned to antisymmetric vibrations (ν_3) of P–O bonds. Signals at 598 and 563 cm^{-1} belong to bending vibrations (ν_4) of O–P–O groups. The peak at 963 cm^{-1} is due to symmetric vibration (ν_1) of P–O bonds. The 473 cm^{-1} component is assigned to ν_2 domain of the PO_4 . The aforementioned vibrations are internal vibrations of PO_4 group characteristic and well defined in the spectrum of pure hydroxyapatite.

The increase in magnesium content in the Mg–CaP samples resulted in the broadening of phosphate bands and a significant reduction in the band intensities that can be related to a decrease in the relative amount of HAP phase and decrease in sample crystallinity. Mg^{2+} incorporation is found to destabilize the hydroxyapatite structure and stabilizes the whitlockite phase. The reduction in the intensity of OH^- vibration bands at 3572 and 630 cm^{-1} is in accordance with the literature data [46, 47]. FTIR spectra of samples with higher magnesium content, 5-Mg-CaP and 10-Mg-CaP, show shoulders at about 1060 cm^{-1} and 990 cm^{-1} . The appearance of low intensity bands at 1136, 922 and 853 cm^{-1} (marked with asterisk in Fig. 4b) is in agreement with whitlockite formation [48], as confirmed by XRD.

Vibrational bands at 1456 and 1413 cm^{-1} assigned to ν_3 mode of CO_3^{2-} and band at 872 cm^{-1} characteristic for ν_2 vibration mode of CO_3^{2-} confirmed B-type carbonate substitution, typical for biological apatites, where CO_3^{2-} dominantly replaces PO_4^{3-} site in the apatite lattice [49–52]. Detailed analysis of the FTIR spectra indicates the presence of a small amount of the A-type-substituted hydroxyapatite as well, where CO_3^{2-} substitutes hydroxyl (OH^-) ions, as well. The band at 1549 cm^{-1} and the very weak signal at 879 cm^{-1} correspond to ν_3 and ν_2 vibrational modes of CO_3^{2-} , distinctive for A-type carbonated hydroxyapatite [50, 53, 54]. It is apparent that the addition of magnesium consequently reduces the intensity of CO_3^{2-} vibrational bands. While ν_2 carbonate vibrational bands seem to show a regular decrease in the intensities, it is not a case with antisymmetric vibrations (ν_3) of carbonate group. As shown in Fig. 4a, the carbonate peak intensity of the sample 5-Mg-CaP is higher compared to the sample 2.5-Mg-CaP. Because of that, the analysis of PO_4^{3-} and CO_3^{2-} peak areas has been performed.

As in the biological and low crystalline samples, the $\nu_1(\text{PO}_4)$ singlet vibration appears as a shoulder and is not clearly separated from the $\nu_3(\text{PO}_4)$, the combined $\nu_1\nu_3(\text{PO}_4)$ domain from 1230–900 cm^{-1} appears to be most practical for relative carbonate quantification. Separation of the $\nu_3(\text{CO}_3)$ vibration mode (1600–1330 cm^{-1}) from the main phosphate absorption bands makes it suitable for relative carbonate quantification. The $\nu_2(\text{CO}_3)$ vibrational mode is not appropriate for the evaluation of carbonate content as the influence of HPO_4^{2-} cannot be excluded without external method of HPO_4^{2-} quantification [55]. The correlation

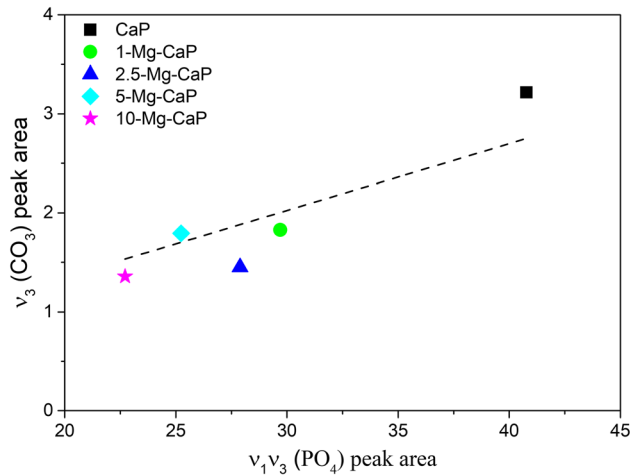


Figure 5 Correlation between $v_1v_3(\text{PO}_4)$ and $v_3(\text{CO}_3)$ integrated peak area derived from vibrational domains of FTIR spectra. Black dash line represents linear data fit with fixed intercept at (0, 0).

between $v_1v_3(\text{PO}_4)$ and $v_3(\text{CO}_3)$ integrated peak areas is shown in Fig. 5. Although the data are scattered, it looks like there might be a linear correlation between the considered peak areas. Black dash line in Fig. 5 represents linear data fit with fixed intercept at (0, 0).

SEM-EDX analysis

The microstructure of the prepared scaffolds was investigated by SEM analysis. As shown in Fig. 6a a layered, cellular quasi-periodic structure of cuttlefish bone consisting of lamellae separated by numerous pillars was maintained after the hydrothermal treatment. The pillars cca. 400 μm high form interconnected channels of width between 50 and 100 μm [34, 37]. At higher magnification, irregularly shaped microspheres with cauliflower morphology, typical for HAP, are observed on the surface of lamellae and pillars of CaP scaffold (Fig. 6a–c).

The addition of Mg ions changed the surface morphology of investigated scaffolds. With the increase of Mg content microspheres become smaller, as clearly visible comparing Fig. 6c–f.

SEM micrographs of the 10-Mg-CaP scaffold show inhomogeneous regions with a different form of agglomerates. Several hexahedral crystals are hardly seen on the cauliflower like surface (Fig. 6g). In Fig. 6h), hollow microspheres are seen.

The energy-dispersive X-ray analysis has been used to determine the atomic composition of prepared scaffolds. EDX spectra (data not shown)

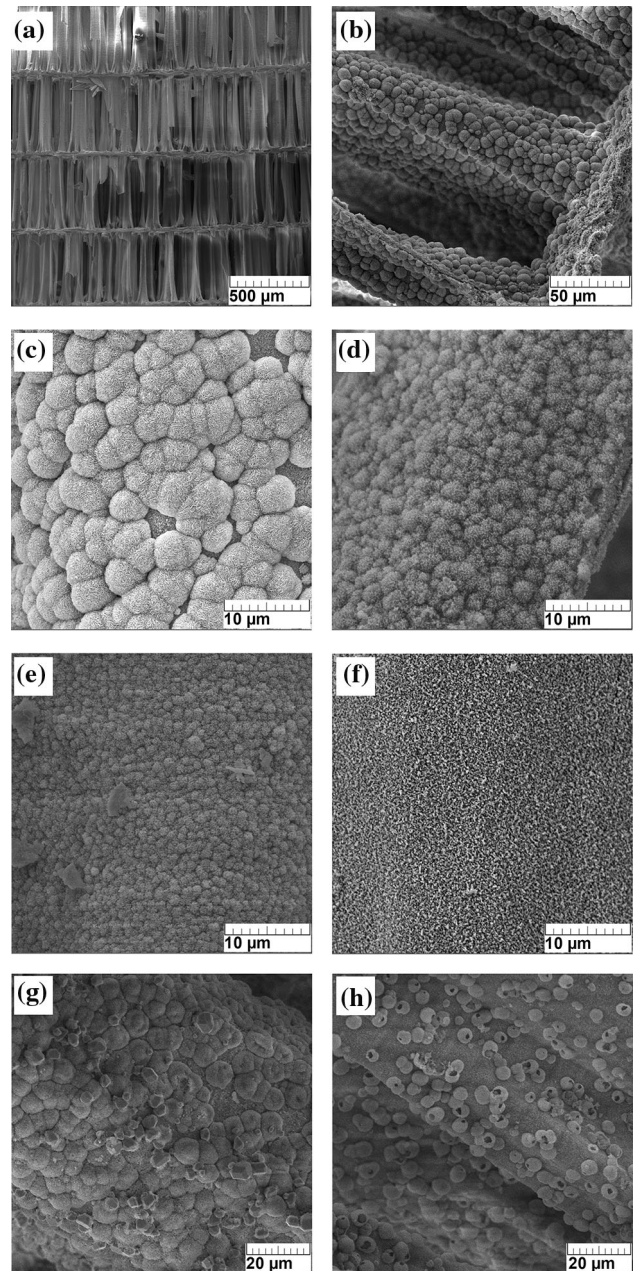


Figure 6 SEM micrographs of the surface of scaffolds: a–c CaP (scale bars: 500, 50 and 10 μm), d 1-Mg-CaP, e 2.5-Mg-CaP, f 5-Mg-CaP (scale bars:10 μm), g and h 10-Mg-CaP (scale bar:20 μm).

confirmed the presence of calcium, phosphorus, oxygen and magnesium. In addition, EDX mapping indicated that calcium, phosphorus, carbon and magnesium were uniformly distributed over the entire investigated area (Fig. 7 a–c). As shown in Fig. 7 d, EDX mapping indicated the presence of Mg even in the CaP scaffold due to biogenic calcium carbonate precursor (cuttlefish bone) that contains

Figure 7 EDX elemental mapping of calcium (a), phosphorus (b) and carbon (c) of the 5-Mg-CaP sample. d–f EDX mapping of magnesium on CaP, 1-Mg-CaP and 5-Mg-CaP samples, respectively.

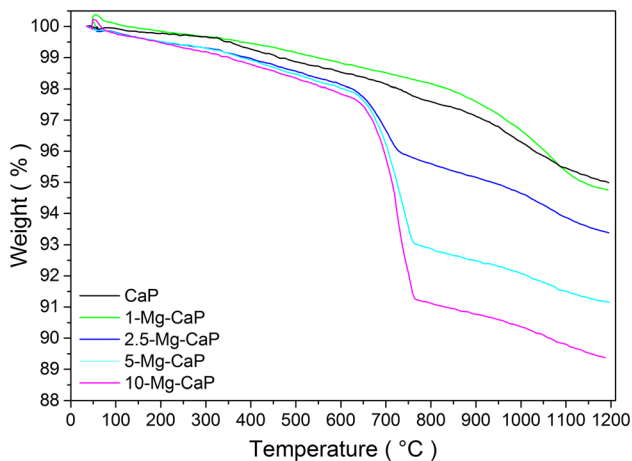
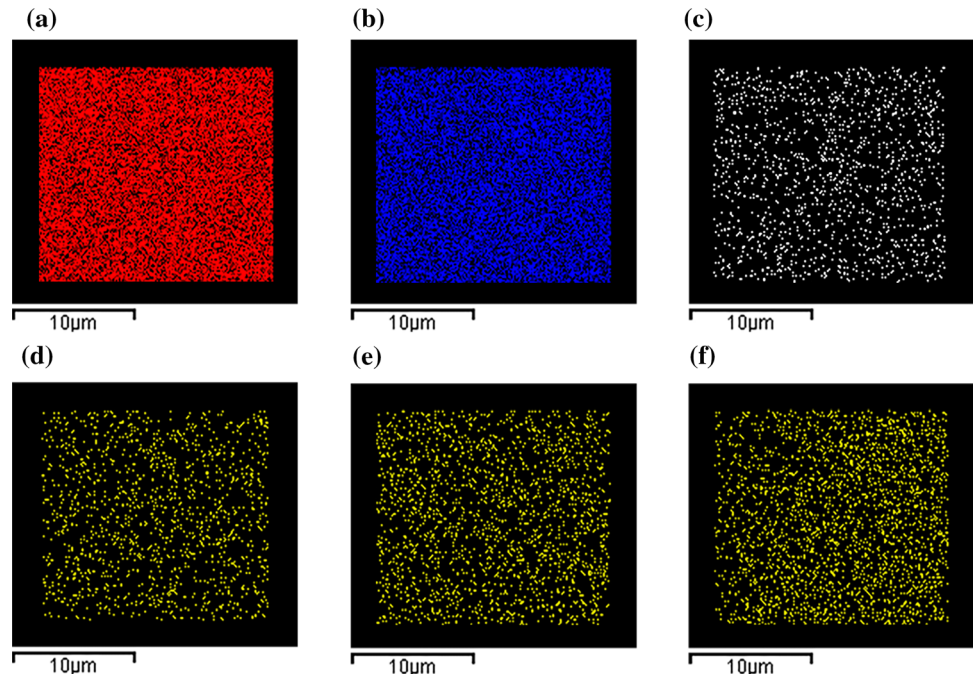


Figure 8 Results of thermogravimetric analysis of prepared samples heated from 40 to 1200 °C in air atmosphere.

Mg as a trace element, as confirmed by inductively coupled plasma mass spectrometry (ICP-MS) in the previous study [38].

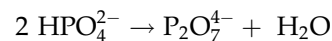
Thermal analysis

Results of thermogravimetric analysis of prepared samples heated from 40 to 1200 °C are shown in Fig. 8.

The scaffolds CaP and 1-Mg-CaP show similar thermal stability with the total weight loss of 5.0 and 5.3 wt%, respectively. With the increase in Mg

content, the total weight loss increases as well, being 6.6, 8.8 and 10.7 wt% for 2.5-Mg-CaP, 5-Mg-CaP and 10-Mg-CaP scaffolds, respectively. The weight loss up to about 350 °C can be attributed to the loss of physically absorbed and lattice (occluded) water. Further gradual weight loss in the CaP scaffold could be attributed to the evolution of CO₂ gas due to the decomposition of carbonate ion substituted for phosphate group in hydroxyapatite, whose presence was confirmed by FTIR.

Scaffolds 2.5-Mg-CaP, 5-Mg-CaP and 10-Mg-CaP show a relevant weight loss around 700 °C due to the release of water formed from the condensation of HPO₄²⁻ ions, incorporated into whitlockite lattice [24] according to the equation:



Cytotoxicity evaluation of extracts

The results of MTT test are presented in Fig. 9 as a percentage of viable HEK293 human embryonic kidney cells treated with sample extracts for 72 h. Estimated cells viability (between 90 and 130% of control) indicates that all prepared scaffolds do not release toxic substances. Cell viability of 1-Mg-CaP scaffolds prepared with chloride or perchlorate precursors showed a similar level of cell viability; however, it is slightly reduced compared to CaP scaffold.

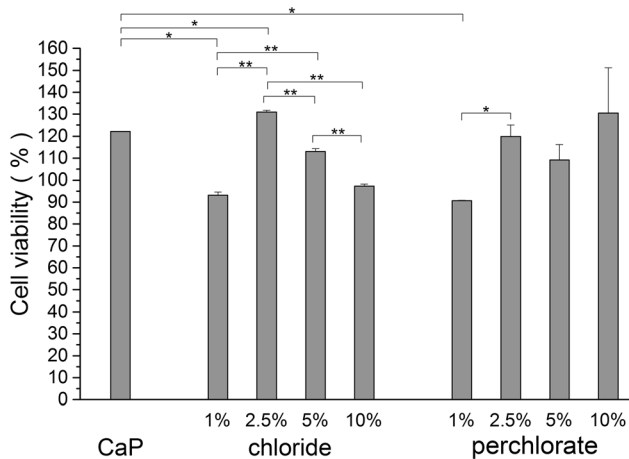


Figure 9 MTT assay of HEK293 human embryonic kidney cell line cultured in extracts of CaP and Mg-CaP samples for 72 h. Extracts were obtained after soaking the samples into the culture medium for 7 days. Mg-CaP samples substituted with magnesium from $\text{MgCl}_2 \times 6\text{H}_2\text{O}$ (chloride) and $\text{Mg}(\text{ClO}_4)_2$ (perchlorate) were used. Data are expressed as a percentage over the control cells, considering the control group as 100% (untreated cells). The significant difference between two groups: * $p < 0.05$; ** $p < 0.01$.

The extracts of scaffolds CaP and 2.5-Mg-CaP indicate to be significantly favourable for cell proliferation.

Immunohistochemical staining of scaffolds

As shown before, a more complete hydrothermal conversion of aragonite was obtained using magnesium perchlorate precursor. Moreover, samples synthesized with magnesium chloride indicated lower HEK293 cells proliferation with higher Mg concentration. Therefore, scaffolds prepared with magnesium perchlorate as Mg precursor were chosen for longer hMSCs culture.

Representative images of immunohistochemical staining for type I collagen and osteocalcin on CaP, 1-Mg-CaP and 5-MgCaP scaffolds after 14 and 21 days of osteogenic induction are shown in Figs. 10,11, respectively.

Brown positive staining (Fig. 10) indicates the appearance of collagen I, secreted from encapsulated hMSC, that prepares extracellular matrix (ECM) for the mineralization process. Negative control sections of each sample (Fig. 10h–m) represent staining interference, originating from scaffold material, and should be excluded during the comparison. Weak collagen type I staining is observed on the CaP

scaffold at 14 days of osteoinduction (Fig. 10a). Moderate staining at day 14 on the 1-Mg-CaP scaffold (Fig. 10b) is stronger than that on the 5-Mg-CaP scaffold (Fig. 10c). Stronger staining is observed on all scaffolds after 21 days (Fig. 10d–f) of osteogenic culture. The 1-Mg-CaP scaffold exhibited the highest expression of collagen forming the ECM of interconnected network structure after 21 days of osteoinduction (Fig. 10e).

The expression of osteocalcin (Fig. 11) is comparable to the appearance of the extracellular matrix, observed by the collagen I staining (Fig. 10). No or very weak immunohistochemical staining of osteocalcin is detected on all scaffolds at 14 days of osteoinduction (Fig. 11a–c) indicating that the mineralization process was in the early stage. Weak staining is observed on CaP scaffold after 21 days of osteoinduction (Fig. 11d), while 5-Mg-CaP scaffold at day 21 exhibited moderate staining for osteocalcin (Fig. 11 f). Strong expression of stained osteocalcin was observed on 1-Mg-CaP scaffold after 21 days of osteoinduction (Fig. 11 e) indicating a fibrillar network structure of mineralized ECM.

Mineralization

Alizarin Red S staining was used to characterize extracellular mineral (calcium) deposition by hMSCs after 14 and 21 days of culture (Fig. 12). Scaffolds without hMSC cells are used as negative controls; thus, the staining visible in Fig. 12a–c represents background staining, originating from scaffold material, and should be excluded from observations on samples with hMSC.

Mineralized bone nodules stained red are visible on all samples after 14 and 21 days (Fig. 12d–i). The stronger intensity of red colour and the greater amount of stained area are expressed on all samples after 21 days (Fig. 12g–i) and indicate the pronounced mineralized matrix formation with time. 1-Mg-CaP samples at days 14 and 21 (Fig. 12e, h, respectively) express a slightly greater amount of mineralized matrix than CaP and 5-Mg-CaP samples.

Quantitative evaluation of osteoinduction

Relative expression of osteogenic markers (Fig. 13) shows that CaP sample has lower expression of genes at day 14 than Mg-CaP samples. After 21 days, higher gene expression is visible on all samples. With

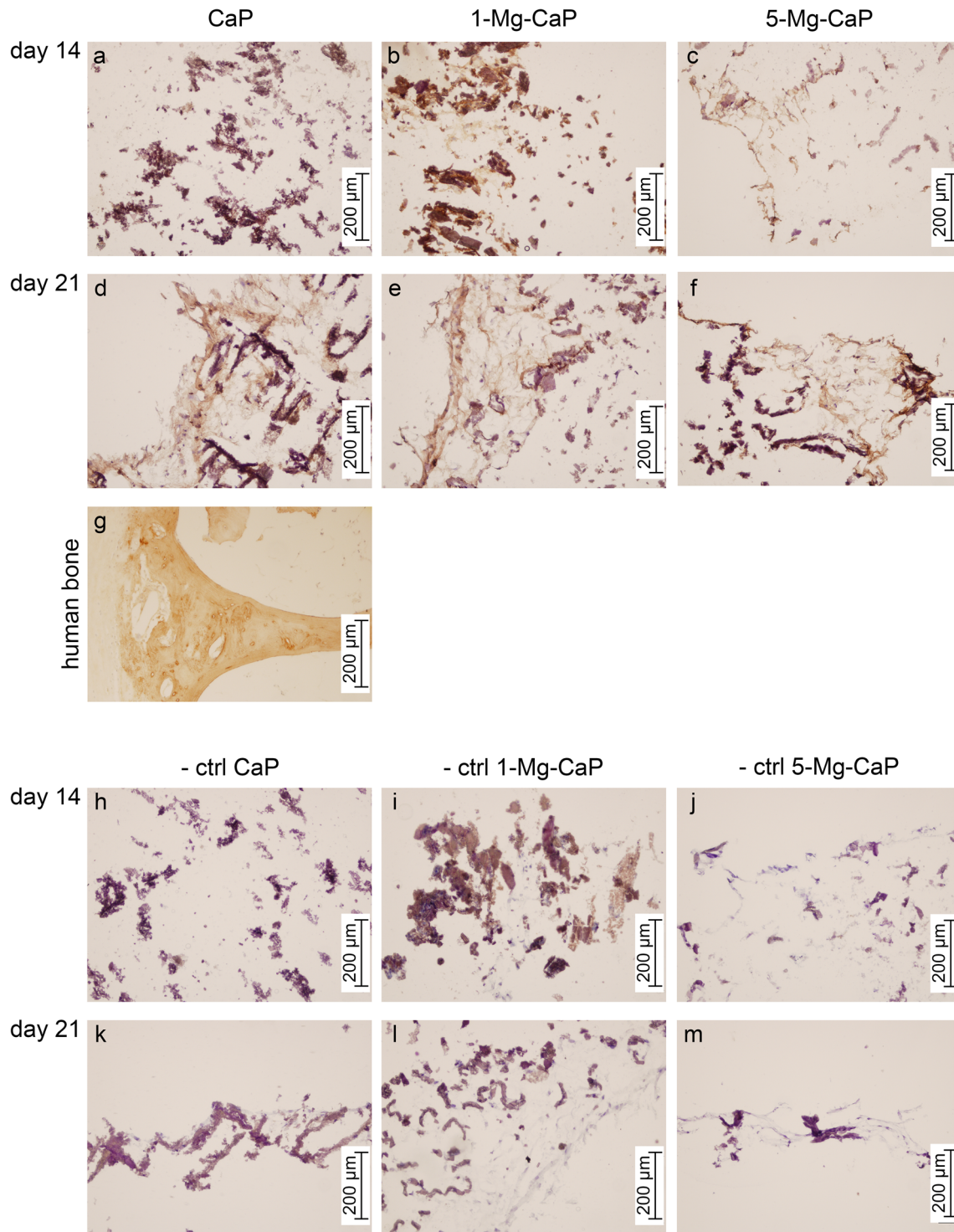


Figure 10 Immunohistochemical examination of collagen type I on CaP, 1-Mg-CaP and 5-Mg-CaP scaffolds after 14 and 21 days of osteogenic induction. Brown colour indicates positive staining. Human bone was used as a sample for the positive control (g). As negative controls (-ctrl of CaP, 1-Mg-CaP and 5-Mg-CaP), sections

were processed for each sample in the absence of the suitable primary antibody (h, i, j, k, l, m). Representative images are shown at 100 × magnification ($n = 3$) and the scale bars represent 200 µm.

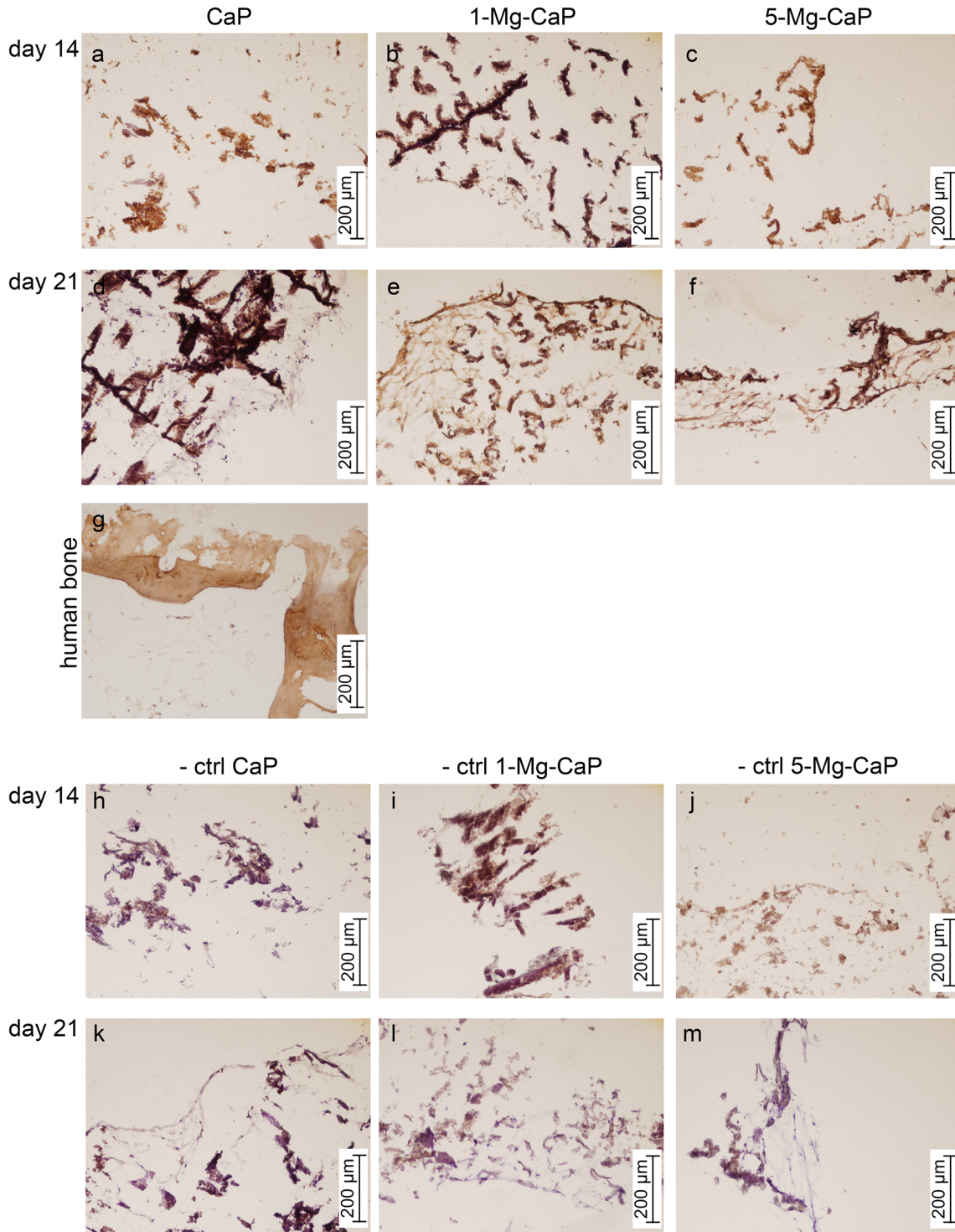


Figure 11 Immunohistochemical examination of osteocalcin on CaP, 1-Mg-CaP and 5-Mg-CaP scaffolds after 14 and 21 days of osteogenic induction. Brown colour indicates positive staining. Human bone was used as a sample for the positive control (g). As negative controls (-ctrl of CaP, 1-Mg-CaP and 5-Mg-CaP), sections

were processed for each sample in the absence of the suitable primary antibody (h, i, j, k, l, m). Representative images are shown at 100 × magnification ($n = 3$) and the scale bars represent 200 µm.

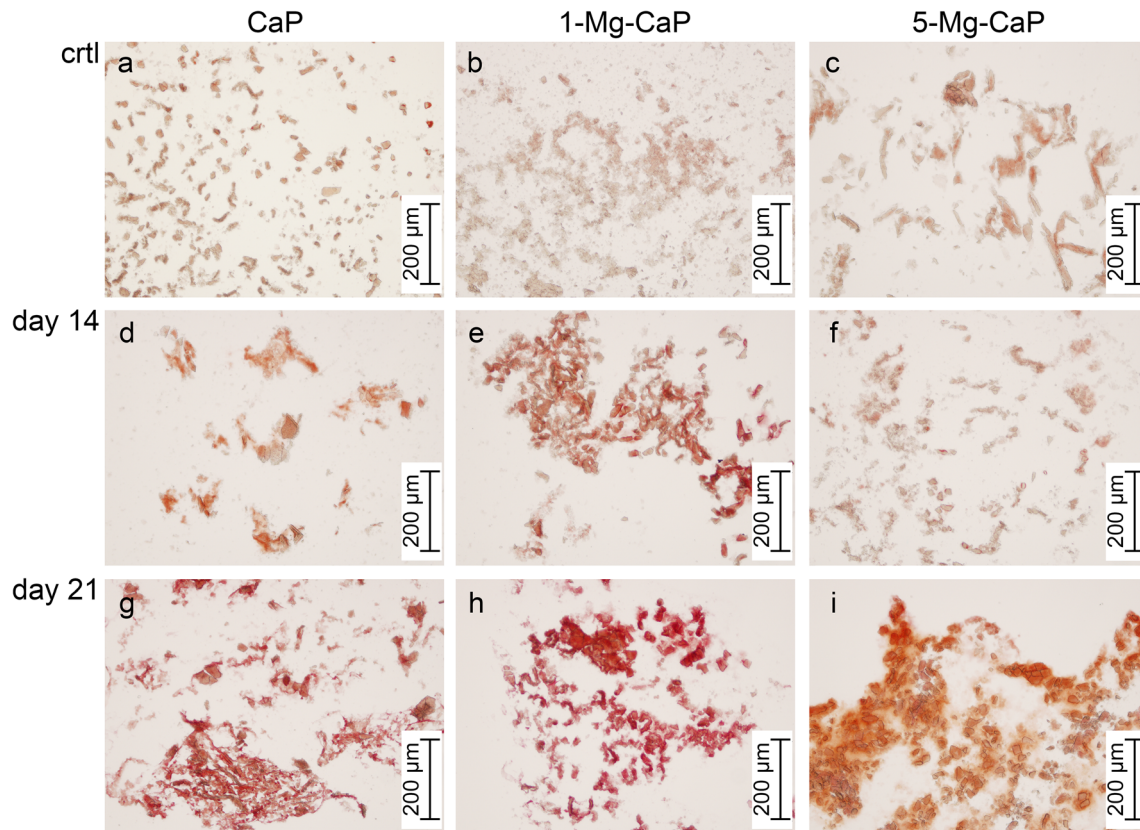


Figure 12 Assessing the mineralization of hMSCs grown in osteogenic medium within CaP, 1-Mg-CaP and 5-Mg-CaP scaffolds after 14 and 21 days. Mineralization of the extracellular matrix with the presence of calcium precipitates was visualized by staining with Alizarin Red S at days 14 and 21.

exception of BSP expression at day 21 for sample 5-Mg-CaP, tested scaffolds do not exhibit significant difference in between later markers of osteoinduction after 21 days of culture.

Mechanical testing

Mechanical properties of the CaP and 1-Mg-CaP scaffolds were evaluated by elastic compression modulus calculated as the slope of the initial linear range of stress–strain curves. The compression modulus of the 1-Mg-CaP scaffold is 48.86 kPa (± 4.57 kPa) and represents a significant increase of stiffness compared to the CaP elastic compression modulus of 21.36 kPa (± 4.80 kPa).

Discussion

In this study, a range of highly porous bone-mimetic scaffolds were prepared by hydrothermal conversion of aragonitic cuttlefish bone in the presence of

Positive staining for calcium is signified by red colour. Representative images are shown at 100 \times magnification ($n = 3$), and the scale bars represent 200 μm . Scaffolds without hMSCs were used as negative controls (ctrl).

Mg^{2+} ion, from two different Mg-sources, magnesium chloride hexahydrate and magnesium perchlorate. Phase composition and microstructure of scaffolds were characterized, and their mechanical and biological properties evaluated.

The XRD analysis showed that the non-substituted CaP scaffold was pure HAP, in accordance with the literature data [35, 37]. The obtained surface charge of CaP (pure HAP) is slightly positively charged (+ 0.085) and much smaller compared to the literature data [34] which indicate surface charge of 0.21. To compensate a charge imbalance in the formula based on the unit-cell contents from Rietveld analysis, the content of OH^- ion was increased from the value of 2.33 (obtained from Rietveld refinements) to 2.54 [34]. The size of CaP (pure HAP) crystallites is similar to those reported previously [34] while Rocha et al. [56] reported the HAP crystallite size range between 20 and 50 nm.

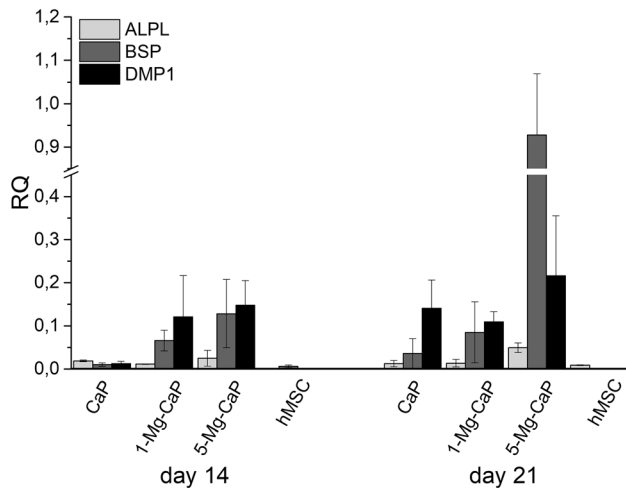


Figure 13 Relative expression (RQ) of osteogenic markers on CaP, 1-Mg-CaP and 5-Mg-CaP scaffolds after 14 and 21 days of osteogenic induction. Quantified osteogenic markers were alkaline phosphatase (ALPL), bone sialoprotein (BSP) and dentin matrix protein 1 (DMP1). Gene expression levels have been normalized to the positive control (human bone). Undifferentiated hMSC represents negative control. β -actin has been used as endogenous reference. The relative expression of target genes was calculated using the comparative cycle threshold method ($\Delta\Delta Ct$).

Sample 1-Mg-CaP was identified as a biphasic mixture, composed of HAP and WH, while samples 2.5-Mg-CaP, 5-Mg-CaP and 10-Mg-CaP, in addition to HAP and WH, contained some quantity of non-transformed aragonite. We assume that the presence of nontransformed aragonite does not have any adverse effect on scaffold properties since some aragonite-based scaffolds are also reported as useful biomedical materials having osteogenic capacity.

Use of magnesium chloride hexahydrate as a precursor resulted in a higher content of nontransformed aragonite in final scaffolds and lower HEK293 cells proliferation, compared to magnesium perchlorate precursor. Because of that, magnesium perchlorate was selected as a more favourable Mg source.

In the literature, there is no consensus on the precise location and configuration of the divalent planar CO_3^{2-} ion substituting for the trivalent tetrahedral phosphate ion in B-type carbonate apatites [57]. Since the proposed carbonate substitution models are not fully convincing, as they are obtained indirectly from a best fit of powder diffraction patterns measured from a limited number of synthetic samples [57], we performed Rietveld refinement using the model without explicit inclusion of CO_3^{2-} ion in the HAP structure. Additional reason why carbonate group

was not included in the refinement is too small difference between X-ray scattering factors for C and P to distinguish between carbon and phosphorous atoms, especially when carbonate level is low [58].

Rietveld refinement was expected to give more information about Mg ion incorporation into the calcium phosphate structures. It was found that different constraints had a negligible effect on the unit-cell dimensions derived from the data (compare Table 4 and Online Resource 3). The lattice parameters and unit-cell volume of HAP in the prepared CaP samples show no systematic change with increased levels of magnesium in the samples, suggesting that no or very limited quantity of Mg^{2+} ions was incorporated into HAP structure. Previous studies [19, 20] showed that Mg substitution for Ca in hydroxyapatite structure occurs only over a limited composition range (up to about 10 wt%), the main portion being surface bound or present in a separate phase.

The refinement of the whitlockite structure revealed a decrease in the lattice parameters a and c , and unit-cell volume with the increase in magnesium content (exception is the sample 5-Mg-CaP), suggesting the substitution of the larger calcium ion (ionic radius 0.99 Å) with the smaller magnesium ion (ionic radius 0.65 Å) that induced a lattice contraction. It should be noted that the Rietveld refinement is not sensitive enough to determine Mg concentration in each (HAP and WH) phase. We attempted to refine both HAP and WH structures with the incorporation of Mg ion on Ca positions inside the crystal structure. Mg occupancies inside the HAP structure in all Mg-CaP samples strived to be a zero; thus, we have not considered it, while calculated occupancies in the WH crystal phase attained values of 0.9363, 0.9863, 1.054 and 1.053 for samples 1-, 2.5-, 5- and 10-Mg-CaP, respectively. Furthermore, considering only basic unit-cell dimensions behaviour, refined unit-cell parameters for each phase indicate that Mg^{2+} ions were preferentially incorporated into the WH phase.

Vibrational bands in FTIR spectra at 1456, 1413 and 872 cm^{-1} confirmed B-type carbonate substitution, where CO_3^{2-} dominantly replaces PO_4^{3-} site in the apatite lattice [49–52]. Since carbonated HAP is closer to the chemical composition of the natural bone mineral than stoichiometrically pure HAP [59] and has been shown experimentally to have enhanced biocompatibility [60, 61], produced scaffolds, with dominantly B-type carbonated HAP, may have great

potential as bone substitutes. The appearance of low intensity bands at 1136, 922 and 853 cm^{-1} is in agreement with formation and increase in WH quantity [48], as confirmed by XRD results.

The addition of magnesium reduced the intensity of CO_3^{2-} vibrational bands of Mg-CaP samples in comparison with pure HAP. We expect that increase in magnesium concentration consequently reduces the intensity of all CO_3^{2-} vibrational bands, both at ν_2 and ν_3 domains. Slight irregularity in the decrease in carbonate group band intensity around 1500 cm^{-1} is observed. A correlation between $\nu_1\nu_3(\text{PO}_4)$ and $\nu_3(\text{CO}_3)$ integrated peak areas was analysed as well. It was found that peak areas of the $\nu_3(\text{CO}_3)$ bands decrease with an increase in Mg content in samples, in a similar way as $\nu_1\nu_3(\text{PO}_4)$ bands do. For any further precise carbonate group quantification, a more detailed method with a validated FTIR methodology like one of A. Grunewald et al (2014) [55] with reference compounds and establishment of calibration curves needs to be developed. It was beyond the scope of this study.

SEM images showed that the interconnected structure of the cuttlefish bone was completely maintained after the hydrothermal synthesis that is beneficial for bone growth and vascularization.

The optimal pore size for bone tissue engineering is still a matter of debate. For successful progression of the bone regeneration process, a minimum pore size between 100 and 150 μm is reported, and for scaffolds with pore size larger than 300 μm enhanced bone formation and vascularization are reported [62]. Our scaffolds featuring high porosity ($\sim 90\%$) and pore size from 50 to 500 μm satisfy the mentioned criteria.

Irregularly shaped microspheres with cauliflower morphology, typical for HAP, are observed on the surface of lamellae and pillars of CaP scaffold (Fig. 6b–c). With the increase in Mg content, microspheres become smaller, as clearly visible comparing Fig. 6c–f. Similar results were also found in the literature [63]. From SEM images, it is difficult to discern between HAP and WH phases. SEM micrographs of the 10-Mg-CaP scaffold, with the highest content of WH phase, show inhomogeneous regions with a different form of agglomerates. Several hexahedral crystals, hardly seen on the cauliflower like surface (Fig. 6g), might be assigned to whitlockite [64]. Hollow microspheres shown in Fig. 6h) are reported for both WH and HAP phases [65, 66]. Qi

et al. [66] prepared WH hollow microspheres by the conventional hydrothermal and microwave-assisted hydrothermal synthesis. Similar hollow structures were observed previously [35] on the HAP scaffold surface, after soaking the scaffold in Hank's balanced salt solution (HBSS).

As mentioned before, Rietveld refinements of XRD data of the sample 10-Mg-CaP indicated high whitlockite content (more than 38 wt%) and a small portion of nontransformed aragonite (around 7 wt%). Formation of magnesium-rich phase crystals on the surface of scaffolds is in the agreement with literature findings [19, 67], showing that skeletal magnesium tends to form a hydrated layer around the hydroxypapatite crystals or to locate in readily exchangeable surface positions.

Thermal analysis of scaffolds 2.5-Mg-CaP, 5-Mg-CaP and 10-Mg-CaP (Fig. 8) showed a rapid decrease in weight around 700 $^\circ\text{C}$ due to the presence of whitlockite phase, confirmed by XRD. Whitlockite ($\text{Ca}_{18}\text{Mg}_2(\text{HPO}_4)_2(\text{PO}_4)_{12}$) loses its HPO_4^{2-} group due to the dehydration and transforms into the magnesium-substituted beta-tricalcium phosphate ($\beta\text{-Ca}_{3-x}\text{Mg}_x(\text{PO}_4)_2$) [22, 26, 27, 42].

Cytotoxicity assays are basic and essential evaluations carried out to determine the biocompatibility of materials which are intended to be used in the biomedical field. However, there is no single standard technique for cytotoxicity assessment. All existing experimental methods to evaluate cytotoxicity have particular problems.

MTT assay has been widely used to assess cell viability and consequentially, cytotoxicity of tested biomaterials. MTT assay is dependent on mitochondrial respiration and indirectly serves to assess the cellular energy capacity.

The mitochondria are maintained at a relatively low activity level in undifferentiated hMSCs, but upon induction of the differentiation process, activity increases [68]. Since mitochondrial properties change during osteogenic differentiation of hMSCs, we have chosen HEK 293 cell line to assess cell viability followed by 72-h sample extracts treatment. HEK 293 cells are the one of the most commonly used cell lines in biomedical and biopharmaceutical research, since they are very easy to grow and maintained offering very high reproducibility. Everything mentioned makes them very preferable over less robust and slow-growing cells like MSC. Thus, we only screened

the potential cytotoxicity of hydroxyapatite/whitlockite scaffold's extracts using HEK 293.

The results of MTT test (estimated cells viability between 90 and 130% of control) indicate that all prepared scaffolds do not release toxic substances. Since scaffolds did not induce reduction in cell viability compared to nontreated cells, further experiments were performed using hMSCs during 14 and 21 days of osteogenic culture, respectively. Biomaterial's preference to support formation of osteoblast was tested by evaluating osteogenic markers on protein and RNA level.

In addition to being non-toxic scaffolds for bone tissue engineering applications should support osteoblast proliferation, their differentiation and ECM mineralization.

One of the earliest stages in hMSC osteogenic differentiation is the production of the type I collagen [69] that can stimulate osteogenic differentiation without additional osteoinductive factors [70]. Collagen I synthesis was confirmed by positive immunohistochemical staining after 14 and 21 days of osteogenic induction (Fig. 10). The presence of whitlockite in HAP/WH scaffolds significantly promoted osteogenic activity of hMSCs, as reported previously [33].

The expression of osteocalcin was found comparable to the appearance of the extracellular matrix, observed by the collagen I staining (Fig. 10 and Fig. 11). Osteocalcin is an extracellular protein produced by osteoblasts indicating the late stage of osteoblast differentiation and matrix mineralization [71–73]. The immunohistochemical staining of osteocalcin after 21 days of culture revealed that the HAP:WH scaffold with WH content of 10 wt% had the most beneficial effect on osteogenesis. The result matched well with the extracellular matrix mineralization detected by alizarin red staining after 14 and 21 days of osteogenic culture.

Quantitative evaluation of osteoinduction complements results of immunohistochemical staining of scaffolds and extracellular mineral deposition. All samples show higher gene expression with time and positive influence of magnesium on osteoinduction from early stage. Both samples, 1-Mg-CaP and 5-Mg-CaP, have expressed osteocalcin and extracellular calcium deposition by hMSC, markers of mineralization.

Alkaline phosphatase is tissue-nonspecific isozyme that plays an important role in skeletal mineralization and development of bones and teeth. ALPL is highly expressed in early stage of osteoinduction and is known as early marker of osteogenesis [74, 75]. ALPL-reduced activity at day 21 indicates later stages of osteoinduction.

BSP and DMP1 are genes characteristic for mineralization and highly expressed in osteocytes; thus, they are classified as later markers of osteoinduction [75, 76]. Considering overall results, RT-qPCR confirms that magnesium in 1-Mg-CaP and 5-Mg-CaP positively influences on differentiation of human mesenchymal cells on porous 3D scaffold.

The major drawback of the CaP scaffolds is their poor mechanical properties, especially the brittleness and low fracture toughness. Considering uncertainty and randomness of samples with structure derived from biogenic sources, our tendency was to prepare samples with representative microstructure. As we already mentioned in "Materials and methods", the use of organisms from the same semi-enclosed marine environment of the same size made it possible to get porous scaffolds with a comparable microstructure. Additionally, as cuttlefish bone has cellular quasi-periodic structure consisting of lamellae and pillars, to avoid the influence of anisotropic scaffold architecture on mechanical properties of 3D scaffold a compressive load perpendicular to lamellae of each specimen has been applied. A significant increase in stiffness of 1-Mg-CaP scaffold compared to CaP scaffold (pure HAP) could be ascribed to the presence of whitlockite phase in biphasic HAP/WH system and a different surface morphology that impact the stress distribution. The result is in accordance with results of Jang et al. [28] who found enhanced mechanical properties of WH bioceramic scaffolds in comparison with HAP scaffolds. However, to be used in load bearing application further improvement in the mechanical properties of the scaffolds is needed. In publications reported by our research group [35, 37], mechanical properties of highly porous CaP scaffolds were improved by a polymer coating. The twofold increase in Young's modulus of 1-Mg-CaP accomplished by Mg^{2+} ions sets a promising foundation for future preparation of ion substituted CaP/polymer composite scaffolds as mechanically adequate bone substitutes.

Conclusions

In this study, a range of porous scaffolds composed of a mixture of carbonated hydroxyapatite and whitlockite, with different HAP:WH ratios, were prepared by hydrothermal conversion of cuttlefish bone. The ratio of HAP:WH phase in biphasic scaffolds can be tailored by the content of Mg ions in the starting solution. Mg ions were preferentially incorporated into the WH phase. Cell culture experiments showed that the Mg-substituted scaffolds are non-cytotoxic. The scaffold with the HAP:WH wt. ratio of 90:10 exhibited higher compressive strength and a higher level of the osteogenic differentiation of hMSC, compared to pure HAP scaffold. In addition, the scaffold with the HAP:WH wt. ratio of 70:30 could also be a good candidate for bone tissue engineering applications.

Acknowledgements

This work has been supported by the Croatian Science Foundation under the project IP-2014-09-3752.

Compliance with ethical standards

Conflict of interest The authors declare that they have no conflict of interest.

Ethical approval Bone marrow-derived hMSCs were used with approval from the Ethical Committee of the University Hospital of Traumatology Zagreb, Croatia, after the written informed consent from donor patients.

Electronic supplementary material: The online version of this article (<https://doi.org/10.1007/s10853-020-05489-3>) contains supplementary material, which is available to authorized users.

References

- [1] Dorozhkin SV (2009) Calcium orthophosphates in nature, biology and medicine. *Materials* 2:399–498
- [2] Dorozhkin SV (2010) Nanosized and nanocrystalline calcium orthophosphates. *Acta Biomater* 6:715–734
- [3] Wang L, Nancollas GH (2008) Calcium orthophosphates: crystallization and dissolution. *Chem Rev* 108:4628–4669
- [4] Le Geros RZ (2008) Calcium phosphate-based osteoinductive materials. *Chem Rev* 108:4742–4753
- [5] Boanini E, Gazzano M, Bigi A (2010) Ionic substitutions in calcium phosphates synthesized at low temperature. *Acta Biomater* 6:1882–1894
- [6] Shepherd JH, Shepherd DV, Best SM (2012) Substituted hydroxyapatites for bone repair. *J Mater Sci Mater Med* 23:2335–2347
- [7] Supova M (2015) Substituted hydroxyapatites for biomedical applications: a review. *Ceram Int* 41:9203–9231
- [8] Tite T, Popa AC, Balescu LM, Bogdan IM, Pasuk I, Ferreira JMF, Stan GE (2018) Cationic substitutions in hydroxyapatite: current status of the derived biofunctional effects and their in vitro interrogation methods. *Materials* 11(11):2081. <https://doi.org/10.3390/ma11112081>
- [9] Si L, Zhang W, Jiang X (2019) Applications of bioactive ions in bone regeneration. *Chin J Dent Res* 22:93–104
- [10] Landi E, Logroscino G, Proietti L, Tampieri A, Sandri M, Sprio S (2008) Biomimetic Mg-substituted hydroxyapatite: from synthesis to in vivo behaviour. *J Mater Sci Mater Med* 19:239–247
- [11] Ren F, Leng Y, Xin R, Ge X (2010) Synthesis, characterization and ab initio simulation of magnesium-substituted hydroxyapatite. *Acta Biomater* 6:2787–2796
- [12] Farzadi A, Bakhshi F, Solati-Hashjin M, Asadi-Eydivand M, Osman NAA (2014) Magnesium incorporated hydroxyapatite: synthesis and structural properties characterization. *Ceram Int* 40:6021–6029
- [13] Yuan XY, Zhu BS, Tong GS, Su Y, Zhu XY (2013) Wet-chemical synthesis of Mg-doped hydroxyapatite nanoparticles by step reaction and ion exchange processes. *J Mater Chem B* 1:6551–6559
- [14] Cox SC, Jamshidi P, Grover LM, Mallick KK (2014) Preparation and characterisation of nanophase Sr, Mg, and Zn substituted hydroxyapatite by aqueous precipitation. *Mater Sci Eng C Mater Biol Appl* 35:106–114
- [15] Stipniece L, Salma-Ancane K, Borodajenko N, Sokolova M, Jakovlevs D, Berzina-Cimdina L (2014) Characterization of Mg-substituted hydroxyapatite synthesized by wet chemical method. *Ceram Int* 40:3261–3267
- [16] Stipniece L, Narkevica I, Salma-Ancane K (2017) Low-temperature synthesis of nanocrystalline hydroxyapatite: effect of Mg and Sr content. *J Am Ceram Soc* 100:1697–1706
- [17] Suchanek WL, Byrappa K, Shuk P, Riman RE, Janas VF, TenHuisen KS (2004) Preparation of magnesium-substituted hydroxyapatite powders by the mechanochemical-hydrothermal method. *Biomaterials* 25:4647–4657
- [18] Batra U, Kapoor S, Sharma S (2013) Influence of magnesium ion substitution on structural and thermal behaviour of

- nanodimensional hydroxyapatite. *J Mater Eng Perform* 22:1798–1806
- [19] Neuman WF, Mulryan BJ (1971) Synthetic hydroxyapatite crystals. *Cal Tissue Res* 7(1):133–138
- [20] Bigi A, Falini G, Foresti E, Gazzano M, Ripamonti A, Roveri N (1993) Magnesium influence on hydroxyapatite crystallization. *J Inorg Biochem* 49:69–78
- [21] Laurencin D, Almora-Barrios N, de Leeuw NH, Gervais C, Bonhomme C, Mauri F, Chrzanowski W, Knowles JC, Newport RJ, Wong A, Gan ZE, Smith ME (2011) Magnesium incorporation into hydroxyapatite. *Biomaterials* 32:1826–1837
- [22] Jang HL, Jin K, Lee J, Kim Y, Nahm SH, Hong KS, Nam KT (2013) Revisiting whitlockite, the second most abundant biomineral in bone: nanocrystal synthesis in physiologically relevant conditions and biocompatibility evaluation. *ACS Nano* 8:634–641
- [23] Jang HL, Lee HK, Jin K, Ahn HY, Lee HE, Nam KT (2015) Phase transformation from hydroxyapatite to the secondary bone mineral, whitlockite. *J Mater Chem B* 3:1342–1349
- [24] Elliott JC (2013) Structure and chemistry of the apatites and other calcium orthophosphates. Elsevier, Amsterdam
- [25] Driessens FC, Verbeeck R (1990) Biomaterials. CRC Press, Florida
- [26] Calvo C, Gopal R (1975) Crystal-structure of whitlockite from Palermo Quarry. *Am Mineral* 60:120–133
- [27] Gopal R, Calvo C (1972) Structural relationship of whitlockite and β -Ca₃(PO₄)₂. *Nat Phys Sci* 237:30–32
- [28] Jang HL, Zheng GB, Park J, Kim HD, Baek HR, Lee HK, Lee K, Han HN, Lee CK, Hwang NS, Lee JH, Nam KT (2016) In vitro and in vivo evaluation of whitlockite biocompatibility: comparative study with hydroxyapatite and β -tricalcium phosphate. *Adv Healthc Mater* 5:128–136
- [29] Kim HD, Jang HL, Ahn HY, Lee HK, Park J, Lee ES, Lee EA, Jeong YH, Kim DG, Nam KT (2017) Biomimetic whitlockite inorganic nanoparticles-mediated in situ remodeling and rapid bone regeneration. *Biomaterials* 112:31–43
- [30] Yoshizawa S, Brown A, Barchowsky A, Sfeir C (2014) Role of magnesium ions on osteogenic response in bone marrow stromal cells. *Connect Tissue Res* 55:155–159
- [31] Chaudhry AA, Goodall JBM, Vickers M, Cockcroft JK, Rehman IU, Knowles JC, Darr JA (2008) Synthesis and characterisation of magnesium substituted calcium phosphate bioceramic nanoparticles made via continuous hydrothermal flow synthesis. *J Mater Chem* 18:5900–5908
- [32] Luna-Domínguez JH, Téllez-Jiménez H, Hernández-Cocoletz H, García-Hernández M, Melo-Banda JA, Nygren H (2018) Development and in vivo response of hydroxyapatite/whitlockite from chicken bones as bone substitute using a chitosan membrane for guided bone regeneration. *Ceram Int* 44:22583–22591
- [33] Cheng H, Chabok R, Guan XF, Chawla A, Li YX, Khademhosseini A, Jang HL (2018) Synergistic interplay between the two major bone minerals, hydroxyapatite and whitlockite nanoparticles, for osteogenic differentiation of mesenchymal stem cells. *Acta Biomater* 69:342–351
- [34] Ivanković H, Gallego Ferrer G, Tkalčec E, Orlić S, Ivanković M (2009) Preparation of highly porous hydroxyapatite from cuttlefish bone. *J Mater Sci Mater Med* 20:1039–1046
- [35] Milovac D, Gallego Ferrer G, Ivanković M, Ivanković H (2014) PCL-coated hydroxyapatite scaffold derived from cuttlefish bone: morphology, mechanical properties and bioactivity. *Mater Sci Eng C* 34:437–445
- [36] Milovac D, Gamboa-Martinez TC, Ivanković M, Gallego Ferrer G, Ivanković H (2014) PCL-coated hydroxyapatite scaffold derived from cuttlefish bone: in vitro cell culture studies. *Mater Sci Eng C* 42:264–272
- [37] Rogina A, Antunović M, Milovac D (2019) Biomimetic design of bone substitutes based on cuttlefish bone-derived hydroxyapatite and biodegradable polymers. *J Biomed Mater Res B* 107:197–204
- [38] Ressler A, Cvetnić M, Antunović M, Marijanović I, Ivanković M, Ivanković H (2020) Strontium substituted biomimetic calcium phosphate system derived from cuttlefish bone. *J Biomed Mater Res B* 108:1697–1709
- [39] TOPAS V4 (2002) General profile and structure analysis software for powder diffraction data-user's manual. Bruker AXS, Karlsruhe
- [40] Sudarsanan K, Young RA (1969) Significant precision in crystal structural details: holly springs hydroxyapatite. *Acta Crystallogr B* 25:1534–1543
- [41] Coelho A (2000) Whole profile structure solution from powder diffraction data using simulated annealing. *J Appl Cryst* 33:899–908
- [42] Gopal R, Calvo C, Ito J, Sabine WK (1974) Crystal structure of synthetic Mg-whitlockite, Ca₁₈Mg₂H₂(PO₄)₁₄. *Can J Chem* 52:1155–1164
- [43] Caspi EN, Pokroy B, Lee PL, Quintana JP, Zolotoyabko E (2005) On the structure of aragonite. *Acta Crystallogr B* 61:129–132
- [44] Matic I, Antunović M, Brkić S, Josipović P, Mihalić KC, Karlak I, Ivković A, Marijanović I (2016) Expression of OCT-4 and SOX-2 in bone marrow-derived human mesenchymal stem cells during osteogenic differentiation. *Open Access Maced J Med Sci* 4:9–16
- [45] Rogina A, Antunović M, Pribolšan L, Caput Mihalić K, Vukasović A, Ivković A, Marijanović I, Gallego Ferrer G, Ivanković M, Ivanković H (2017) Human mesenchymal stem cells differentiation regulated by hydroxyapatite

- content within chitosan-based scaffolds under perfusion conditions. *Polymers* 9(9):387. <https://doi.org/10.3390/polym9090387>
- [46] Zyman Z, Tkachenko M, Epple M, Polyakov M, Naboka M (2006) Magnesium-substituted hydroxyapatite ceramics. *Materialwiss Werkstofftech* 37:474–477
- [47] Mehrjoo M, Javadpour J, Shokrgozar MA, Farokhi M, Javadian S, Bonakdar S (2015) Effect of magnesium substitution on structural and biological properties of synthetic hydroxyapatite powder. *Mater Expr* 5:41–48
- [48] Aina V, Lusvardi G, Annaz B, Gibson IR, Imrie FE, Malavasi G, Menabue L, Cerrato G, Martra G (2012) Magnesium- and strontium-co-substituted hydroxyapatite: the effects of doped-ions on the structure and chemico-physical properties. *J Mater Sci Mater Med* 23:2867–2879
- [49] LeGeros RZ (1991) Calcium phosphates in oral biology and medicine. In: LeGeros RZ, Myers HM (eds) *Monographs in Oral Sciences*. Karger, Basel, pp 37–58
- [50] El Feki H, Rey C, Vignoles M (1991) Carbonate ions in apatites: infrared investigations in the ν_4 CO₃ domain. *Calcif Tissue Int* 49:269–274
- [51] Elliott JC, Holcomb DW, Young RA (1985) Infrared determination of the degree of substitution of hydroxyl by carbonate ions in human dental enamel. *Calcif Tissue Int* 37:372–375
- [52] Rey C, Collins B, Goehl T, Dickson IR, Glimcher MJ (1989) The carbonate environment in bone-mineral—a resolution enhanced Fourier-transform infrared-spectroscopy study. *Calcif Tissue Int* 45:157–164
- [53] Bonel G (1972a) Contribution a l'étude de la carbonation des apatites. Part I *Ann Chim* 7:65–87
- [54] Bonel G (1972b) Contribution a l'étude de la carbonation des apatites. Parts II and III *Ann Chim* 7:127–144
- [55] Grunenwald A, Keyser C, Sautereau AM, Crubézy E, Ludes B, Drouet C (2014) Revisiting carbonate quantification in apatite (bio)minerals: a validated FTIR methodology. *J Archaeol Sci* 49:134–141
- [56] Rocha JHG, Lemos AF, Agathopoulos S, Kannan S, Valério P, Ferreira JMF (2006) Hydrothermal growth of hydroxyapatite scaffolds from aragonitic cuttlefish bones. *J Biomed Mater Res Part A* 77:160–168
- [57] Leventouri T (2006) Synthetic and biological hydroxyapatites: crystal structure questions. *Biomaterials* 27:3339–3342
- [58] Tkalčec E, Popović J, Orlić S, Milardović S, Ivanković H (2014) Hydrothermal synthesis and thermal evolution of carbonate-fluorhydroxyapatite scaffold from cuttlefish bones. *Mater Sci Eng C* 42:578–586
- [59] Bigi A, Cojazzi G, Panzavolta S, Ripamonti A, Roveri N, Romanello M, Suarez KN, Moro L (1997) Chemical and structural characterization of the mineral phase from cortical and trabecular bone. *J Inorg Biochem* 68:45–51
- [60] Wopenka B, Pasteris JD (2005) A mineralogical perspective on the apatite in bone. *Mater Sci Eng C* 25:131–143
- [61] Ellies LG, Carter JM, Natiella JR, Featherstone JDB, Nelson DGA (1988) Quantitative analysis of early in vivo tissue response to synthetic apatite implants. *J Biomed Mater Res A* 22:137–148
- [62] Karageorgiou V, Kaplan D (2005) Porosity of 3D biomaterial scaffolds and osteogenesis. *Biomaterials* 26:5474–5491
- [63] Tampieri A, Celotti GC, Landi E, Sandri M (2004) Magnesium doped hydroxyapatite: synthesis and characterization. *Key Eng Mater* 264:2051–2054
- [64] Tas AC (2016) Transformation of Brushite (CaHPO₄·2H₂O) to Whitlockite (Ca₉Mg(HPO₄)(PO₄)₆) or other CaPs in physiologically relevant solutions. *J Am Ceram Soc* 99:1200–1206
- [65] Qi C, Chen F, Wu J, Zhu Y-J, Hao C-N, Duan J-L (2016) Magnesium whitlockite hollow microspheres: a comparison of microwave-hydrothermal and conventional hydrothermal syntheses using fructose 1,6-bisphosphate, and application in protein adsorption. *RSC Adv* 6:33393–33402
- [66] Qi C, Zhu YJ, Lu BQ, Zhao XY, Zhao J, Chen F, Wu J (2013) Hydroxyapatite hierarchically nanostructured porous hollow microspheres: rapid, sustainable microwave-hydrothermal synthesis by using creatine phosphate as an organic phosphorus source and application in drug delivery and protein adsorption. *Chem Eur J* 19:5332–5341
- [67] Mouriño V, Cattalini JP, Boccaccini AR (2012) Metallic ions as therapeutic agents in tissue engineering scaffolds: an overview of their biological applications and strategies for new developments. *J R. Soc Interface* 9:401–419
- [68] Li QQ, Gao ZW, Chen Y, Guan MX (2017) The role of mitochondria in osteogenic, adipogenic and chondrogenic differentiation of mesenchymal stem cells. *Protein Cell* 28:439–445
- [69] Takeuchi Y, Suzawa M, Kikuchi T, Nishida E, Fujita T, Matsumoto T (1997) Differentiation and transforming growth factor- β receptor down-regulation by collagen- α 2 β 1 integrin interaction is mediated by focal adhesion kinase and its downstream signals in murine osteoblastic cells. *J Biol Chem* 272:29309–29316
- [70] Kundu AK, Putnam AJ (2006) Vitronectin and collagen I differentially regulate osteogenesis in mesenchymal stem cells. *Biochem Biophys Res Commun* 347:347–357
- [71] Stein GS, Lian JB, Stein JL, Van Wijnen AJ, Montecino M (1996) Transcriptional control of osteoblast growth and differentiation. *Physiol Rev* 76:593–629
- [72] Stein GS, Lian JB, Van Wijnen AJ, Stein JL (1997) The osteocalcin gene: A model for multiple parameters of

- skeletal-specific transcriptional control. *Mol Biol Rep* 24:185–196
- [73] Gundberg CM (2000) Biochemical markers of bone formation. *Clin Lab Med* 20:489–501
- [74] Golub EE, Boesze-Battaglia K (2007) The role of alkaline phosphatase in mineralization. *Curr Opin Orthop* 18:444–448
- [75] Rad MR, Liu D, He H, Brooks H, Xiao M, Wise GE, Yao S (2015) The role of dentin matrix protein 1 (DMP1) in regulation of osteogenic differentiation of rat dental follicle stem cells (DFSCs). *Arch Oral Biol* 60:546–556
- [76] Gordon JA, Tye CE, Sampaio AV, Underhill TM, Hunter GK, Goldberg HA (2007) Bone sialoprotein expression enhances osteoblast differentiation and matrix mineralization in vitro. *Bone* 41:462–473

Publisher's Note Springer Nature remains neutral with regard to jurisdictional claims in published maps and institutional affiliations.